Profilin Directly Promotes Microtubule Growth through Residues Mutated in Amyotrophic Lateral Sclerosis

Highlights

- Profilin directly enhances microtubule growth rates *in vitro*

- Evolutionarily diverse profilin homologs stimulate microtubule growth

- Wild-type profilin expression increases microtubule growth rate in cells

- ALS-linked profilin mutants impair microtubule effects *in vitro* and *in vivo*

Authors

Jessica L. Henty-Ridilla, M. Angeles Juanes, Bruce L. Goode

Correspondence

goode@brandeis.edu

In Brief

Henty-Ridilla et al. demonstrate that the actin-binding protein profilin directly enhances microtubule growth rate *in vitro* and in cells. These stimulatory effects on microtubules are unaffected by mutations in profilin disrupting its actin functions and instead rely on surface residues of profilin mutated in ALS patients.

CrossMark

CellPress

Report

Profilin Directly Promotes Microtubule Growth through Residues Mutated in Amyotrophic Lateral Sclerosis

Jessica L. Henty-Ridilla,[1,2] M. Angeles Juanes,[1] and Bruce L. Goode[1,3,*]
[1]Department of Biology, Brandeis University, 415 South Street, Waltham, MA 02454, USA
[2]Present address: Department of Cell and Developmental Biology, 750 East Adams Street, Syracuse, NY 13210, USA
[3]Lead Contact
*Correspondence: goode@brandeis.edu
https://doi.org/10.1016/j.cub.2017.10.002

SUMMARY

Profilin is an abundant actin monomer-binding protein with critical actin regulatory roles *in vivo* [1, 2]. However, profilin also influences microtubule dynamics in cells, which may be mediated in part through its interactions with formins that in turn bind microtubules [3, 4]. Specific residues on human profilin-1 (PFN1) are mutated in patients with amyotrophic lateral sclerosis (ALS) [5, 6]. However, the observation that some ALS-linked PFN1 mutants fail to alter cellular actin organization or dynamics [5–8] or *in vitro* actin-monomer affinity [9] has been perplexing, given that profilin is best understood as an actin regulator. Here, we investigated direct effects of profilin on microtubule dynamics and whether ALS-linked mutations in PFN1 disrupt such functions. We found that human, fly, and yeast profilin homologs all directly enhance microtubule growth rate by several-fold *in vitro*. Microtubule stimulatory effects were unaffected by mutations in the canonical actin- or poly-proline-binding sites of profilin. Instead, microtubule activities depended on specific surface residues on profilin mutated in ALS patients. Furthermore, microtubule effects were attenuated by increasing concentrations of actin monomers, suggesting competition between actin and microtubules for binding profilin. Consistent with these biochemical observations, a 2-fold increase in the expression level of wild-type PFN1, but not the ALS-linked PFN1 mutants, increased microtubule growth rates in cells. Together, these results demonstrate that profilin directly enhances the growth rate of microtubules. They further suggest that ALS-linked mutations in PFN1 may perturb cellular microtubule dynamics and/or the coordination between the actin and microtubule cytoskeletons, leading to motor neuron degeneration.

RESULTS AND DISCUSSION

Profilin is an abundant cytosolic protein with two canonical binding sites, one for actin monomers and one for poly-L-proline

(PLP) tracts found in key actin regulators such as formins and Ena/VASP [10–15]. Through these two interactions, profilin enhances the growth rate of actin filaments [1, 16, 17] and plays a critical role in distributing monomers between different actin nucleation systems [2, 13, 14, 18, 19]. In addition to its well-established roles in regulating actin dynamics, profilin can influence microtubule (MT) organization and dynamics *in vivo* [4, 20]. Further, tubulin and MT-associated proteins have been identified as potential profilin binding partners on affinity columns [19], and profilin has been visualized on the sides of MTs in cells using immunofluorescence following extraction to remove unbound cytosolic profilin [4]. Recent *in vivo* studies suggest that some of these MT regulatory effects may be indirect, mediated by interactions between profilin and formins, which in turn bind MTs [4, 20, 21]. However, whether profilin has direct effects MT dynamics remains an open question.

Human Profilin Directly Enhances the Growth Rate of Microtubules *In Vitro*

We used total internal reflection fluorescence (TIRF) microscopy to compare MT dynamics in the presence and absence of purified human profilin-1 (PFN1) (Figures 1A and 1B; Movie S1). In control reactions, MTs exhibited hallmark characteristics of MT dynamic instability, stochastically transitioning between phases of steady growth and rapid shortening (Figure 1A). Addition of 5 μM PFN1 led to a 4.5-fold increase in MT growth rate (Figures 1B and 1C) but did not change the average time MTs spent growing (Figure 1D). Consistent with an increased growth rate, MTs had increased lengths before undergoing catastrophe in the presence of PFN1 (Figure 1E). PFN1 did not significantly change the frequency of MT catastrophe or rescue events and therefore did not substantially alter MT stability index (ratio of rescue to catastrophe events) (Figure 1F). Enhancement of MT growth was saturated at PFN1 concentrations ≥5 μM, which is well within the physiological concentration range of profilin (Figures 1G and S1A–S1E) [16, 19].

PFN1 also altered the rate of MT elongation over a range of tubulin concentrations (1–30 μM) (Figures 1H and S1F–S1J). From these observations, we calculated that PFN1 increases the on rate of tubulin at MT ends by as much as 4.6-fold (from 3,526 to 16,315 tubulin dimers min^{-1} μM^{-1}). At 5 μM tubulin, significant growth from MT seeds was observed only in the presence of PFN1 (Figure 1I), suggesting that PFN1 also may lower the critical concentration for tubulin polymerization. Consistent with these effects on MT dynamics, purified PFN1 bound to
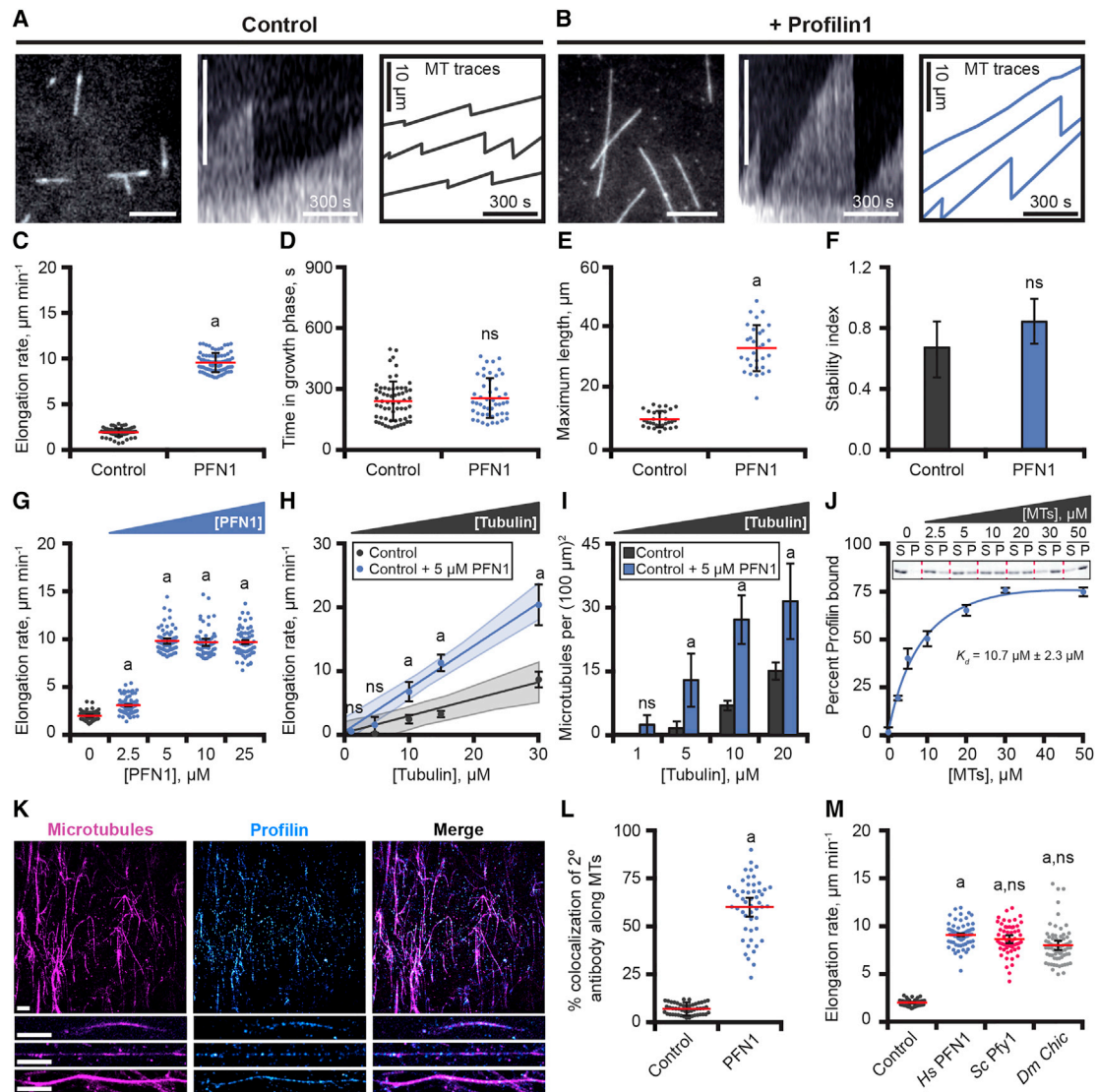
Figure 1. Profilin Increases the Elongation Rate of Microtubules *In Vitro*

(A) Representative field of view from a control TIRF reaction containing biotinylated GMP-CPP MT seeds and 10 μM free tubulin (30% Alexa-647-labeled) (left), with kymograph (middle) and MT length traces (right) showing stochastic growth and shortening of MTs.

(B) Representative fields of view for reactions as in (A) except in the presence of 5 μM wild-type PFN1. Length scale bars, 10 μm. Time scale bars, 300 s.

(C) MT elongation rates from TIRF reactions as in (A) and (B), with and without 5 μM PFN1 (n = 73 MTs per condition).

(D) Duration of growth phase for individual MT elongation events (n = 47–62 MTs per condition).

(E) Maximum length to which MTs grew before undergoing catastrophe (n = 30 MTs per condition).

(F) MT stability index: rescue/catastrophe frequency (measured from n = 50 MTs per condition). Error bars, SE.

(G) MT elongation rates measured in TIRF assays as in (A) at variable concentrations of PFN1 (n = 69–78 MTs per condition).

(H) Linear regression of MT elongation rates from TIRF assays as in (A) at variable concentrations of free tubulin, with and without 5 μM PFN1 (n = 30–73 MTs per condition). Shaded areas represent 95% confidence intervals and error bars indicate SE.

(I) Total number of MTs present in reactions as in (H) (measured from n = 3 reactions per condition).

(J) Inset: representative Coomassie-stained SDS-PAGE gel of supernatants and pellets from MT co-sedimentation assay containing 5 μM PFN1 and variable concentrations of MTs (0–50 μM), with corresponding binding curve.

(K) Field of view from TIRF reactions containing biotinylated GMP-CPP MT seeds, 10 μM free tubulin (30% Alexa-647-labeled), and 5 μM PFN1. MTs were fixed with 0.1% glutaraldehyde and PFN1 was visualized by immunofluorescence. Magnified view of individual MTs decorated by PFN1 are shown below each field of view. Scale bars, 10 μm.

(L) Quantification of PFN1 fluorescence along MTs by line scan analysis, from reactions as in (K) (n = 50 MTs per condition).

(M) MT elongation rates from TIRF reactions performed as in (A) in the presence or absence of 5 μM human PFN1 (blue), *S. cerevisiae* profilin (*Pfy1*) (pink), or *D. melanogaster* profilin (*Chickadee*) (gray) (n = 57–72 MTs per condition). Error bars indicate 95% confidence intervals except where noted. Significant differences by one-way ANOVA with Bartlett's correction for variance: ns, not significantly different from control; a, compared with control ($p < 0.05$); b, compared with PFN1 ($p < 0.05$).

See also Figure S1 and Movies S1 and S2.

MTs in a concentration-dependent manner with an affinity ($K_d = 10.7 \pm 2.3$ μM) that is predicted to readily support binding at physiological concentrations of profilin and tubulin (Figure 1J). Under these same experimental conditions, PFN1 and MTs co-localized by immunofluorescence, supporting a direct interaction (Figures 1K and 1L). Attempts to reengineer profilin surface cysteines to enable fluorescence labeling compromised MT stimulatory functions, precluding live-imaging of profilin interacting with MTs *in vitro*.

We also compared the effects on MTs of purified human PFN1, *S. cerevisiae* profilin (Pfy1), and *D. melanogaster* profilin (Chickadee). Each profilin homolog had similar effects on average MT growth rate and length (Figures 1M and S1K–S1O; Movie S2), demonstrating that MT interactions are conserved among evolutionarily distant members of the profilin family.

ALS-Linked Mutations in Human Profilin Disrupt Microtubule Interactions In Vitro

We next asked whether the MT stimulatory effects of PFN1 are disrupted by mutations in the conserved binding sites for actin monomers (R88E) or poly-L-proline motifs (Y6D) (Figures 2A and 2B) [8]. Both mutants were indistinguishable from wild-type PFN1 in stimulating MT growth (Figures 2B and S1P–S1T). Thus, neither canonical binding site is required for MT interactions. This led us to consider whether surfaces on profilin mutated in ALS might be involved in regulating MT dynamics [5, 6]. The ALS-linked mutations in PFN1 are dominant in patients, and their expression over endogenous PFN1 in cultured primary neurons results in ALS-like phenotypes, including increased stress granule formation [22], impaired neurite outgrowth [5, 7], and motor neuron degeneration [7]. It has remained an open question how some PFN1 mutations (i.e., M114T and G118V) promote neurodegeneration without altering cellular morphology, actin cytoskeleton dynamics [5, 7, 8], or *in vitro* actin monomer binding affinity [9].

We purified four ALS-linked PFN1 mutants (M114T, E117G, G118V, and H120E) that are less prone to aggregation compared to mutations such as C71G [5, 7, 9, 22–24]. Among these mutants, only one (H120E) has shown defects in actin monomer binding [5, 9, 25]. Using *in vitro* TIRF microscopy assays, two mutants (M114T and G118V) completely failed to enhance MT growth, and a third (E117G) exhibited partial defects in stimulating MT growth (Figures 2C, 2D, and S2A). Similar to wild-type PFN1, the mutants did not alter any other parameters of MT dynamics (Figures 2E, 2F, and S2B–S2D). Additionally, M114T and G118V both failed to bind MTs, suggesting that their inability to stimulate MT growth stems from a loss of MT binding affinity. However, the E117G and H120E mutants bound to MTs with affinities similar to wild-type PFN1 (Figures 2G, 2H, S2E, and S2F). Therefore, the partial defects of E117G in stimulating MT growth do not appear to stem from a simple loss of MT affinity (Figures 2G and 2H), but rather a mechanistic defect in MT regulation that we do not yet understand. Because H120E was indistinguishable from wild-type PFN1 in its ability to bind and enhance MT growth, this mutant appears to be impaired specifically in actin binding. An examination of the positions of the MT-defective ALS mutations on PFN1 (M114T, E117G, and G118V) revealed that together they form a surface-exposed patch that is adjacent to, but not overlapping with the actin-binding surface (Figure 2A).

Profilin Effects on Microtubules Are Sensitive to the Presence of Actin Monomers

To further investigate the relationship between the interaction of profilin with MTs and actin, we asked whether PFN1 stimulation of MT growth *in vitro* is affected by increasing concentrations of actin monomers maintained in a monomeric state by Latrunculin-A (Figures 3A and 3B). Latrunculin-A binds to monomeric actin near the nucleotide-binding pocket and does not overlap with the profilin binding footprint on actin [26]. In the presence of 2.5 and 5 μM monomeric actin, 5 μM PFN1 continued to promote MT growth similar to control reactions lacking actin (Figure 3B). However, with 10 μM actin monomers present, PFN1 effects on MT growth were decreased, and with 15 μM actin monomers, the effects of PFN1 on MTs were strongly inhibited. Importantly, the presence of actin only affected those parameters of MT dynamics regulated by PFN1 in the absence of actin (i.e., MT elongation rate and length) (Figures 3B and S3A–S3D). As expected, the Y6D mutant PFN1, which binds normally to actin, had MT regulatory effects sensitive to actin monomers, similar to wild-type PFN1 (Figure 3C). In contrast, the R88E mutant, which is defective in actin binding, stimulated MT growth in a manner that was insensitive to actin monomers (Figure 3D). The M114T and G118V mutants of PFN1 failed to enhance MT growth on their own, or in the presence of actin monomers (Figures 3E and 3F). The E117G mutant showed a modest increase in sensitivity to actin monomer levels compared to wild-type PFN1 (Figure 3G), consistent with its partial defects in MT regulation. Finally, the H120E mutant was almost completely insensitive to actin monomers, consistent with its defects in actin binding (Figure 3H).

Altogether, these dose-response effects (Figure 3I) suggest there is competition between MTs and actin monomers for binding profilin, and this agrees well with the close proximity of the MT and actin-binding sites on profilin (Figure 2A). Further, the observation that half-maximal MT stimulatory effects occurred at equal molar concentrations of tubulin and actin (10 μM each) indicates that profilin has a similar effective concentration range for influencing MTs and actin, consistent with a role in coordinating MT and actin dynamics in cells.

Profilin Increases the Growth Rate of Microtubules in Cells

To test the biological relevance of these observations, we asked whether a modest increase in expression levels of PFN1 alters MT dynamics in mouse neuroblastoma (N2A) cells. Expression of PFN1 led to 2-fold higher levels of PFN1 compared to control cells, as indicated by both quantitative immunofluorescence (Figures S4A–S4C) and quantitative western blot (Figure S4D). The overall fluorescence levels of actin filaments (F-actin) and MTs were not significantly different compared to control cells (Figures S4E and S4F), indicating that cytoskeletal architecture is not grossly altered by elevated PFN1 expression. However, quantitative tracking of MT plus ends (Figures 4A and 4B) revealed an almost 3-fold increase in the average velocity of MT plus ends in cells expressing wild-type PFN1 (Figure 4B). This change in MT dynamics occurred without a change in total MT polymer levels, indicating that PFN1 alters MT dynamics in cells without significantly changing the fraction of tubulin in polymer. Similar results were observed for increased expression of the
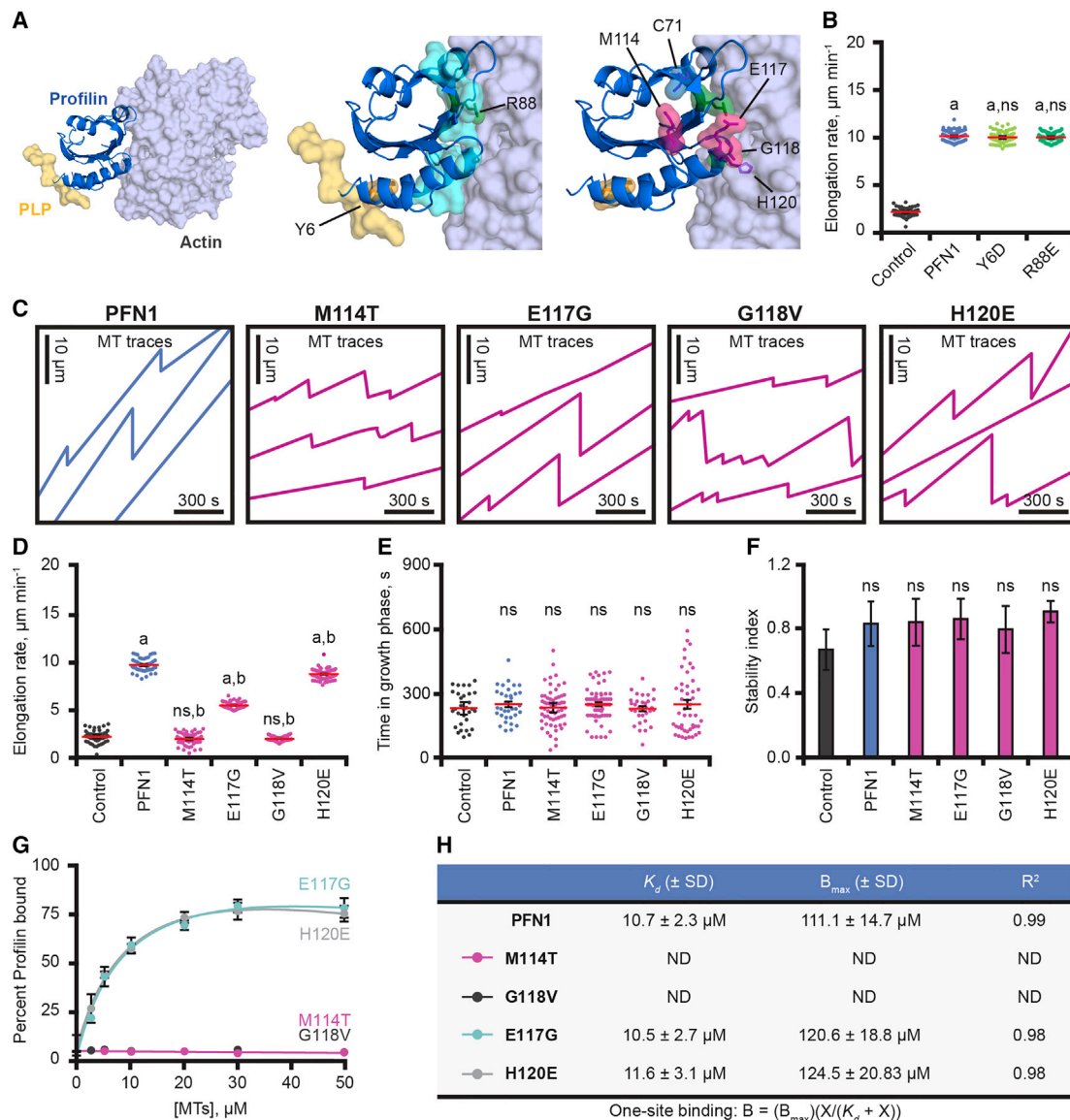
Figure 2. Effects of ALS-Associated Profilin Mutants on Microtubules *In Vitro*

(A) Left: view of profilin (blue) interacting with actin (gray) and with the poly-L-proline (PLP) region of VASP (yellow), modeled using PDB: 2PAV [15] and PDB: 2BTF [10]. Middle: magnified view showing profilin surfaces contacting actin (cyan) and PLP (yellow) and highlighting the positions of key residues required for actin-binding (R88; green) and PLP-binding (Y6; orange). Right: close up view of profilin highlighting the positions of five ALS-linked residues: C71 (blue), mutations in which lead to protein aggregation; H120 (purple), which mediates actin-binding; and M114, E117, and G118, which mediate MT binding and regulation.

(B) MT elongation rates from TIRF reactions containing biotinylated GMP-CPP MT seeds and 10 μM free tubulin (30% Alexa-647-labeled), in the presence and absence of 5 μM wild-type (blue), Y6D (chartreuse), or R88E (green) human PFN1 (n = 66–77 MTs per condition).

(C) Representative MT length traces from TIRF reactions containing biotinylated GMP-CPP MT seeds and 10 μM free tubulin (30% Alexa-647-labeled) in the absence (control) or presence of 5 μM wild-type or ALS mutant PFN1s.

(D) MT elongation rates measured from TIRF reactions in the presence and absence of 5 μM wild-type or ALS mutant PFN1s (n = 50–83 MTs per condition).

(E) Time MTs spent growing before undergoing catastrophe (n = 50 MTs per condition).

(F) MT stability index: number of rescue events/number of catastrophe events. Error bars, SE/

(G) Binding of 5 μM wild-type or ALS mutants of PFN1 to variable concentrations of MTs in co-sedimentation assays (n = 3 replicates per concentration). Error bars, SE.

(H) Table of binding data from co-sedimentation analyses as in (G) comparing wild-type and ALS mutant PFN1s. One-site binding parameters and fit-values for MT binding are derived from the curve fits in (G). All experiments were performed from at least three times. Error bars indicate 95% confidence intervals except where noted. Significant differences by one-way ANOVA with Bartlett's correction for variance: ns, not significantly different from control; a, compared with control ($p < 0.05$); b, compared with PFN1 ($p < 0.05$).

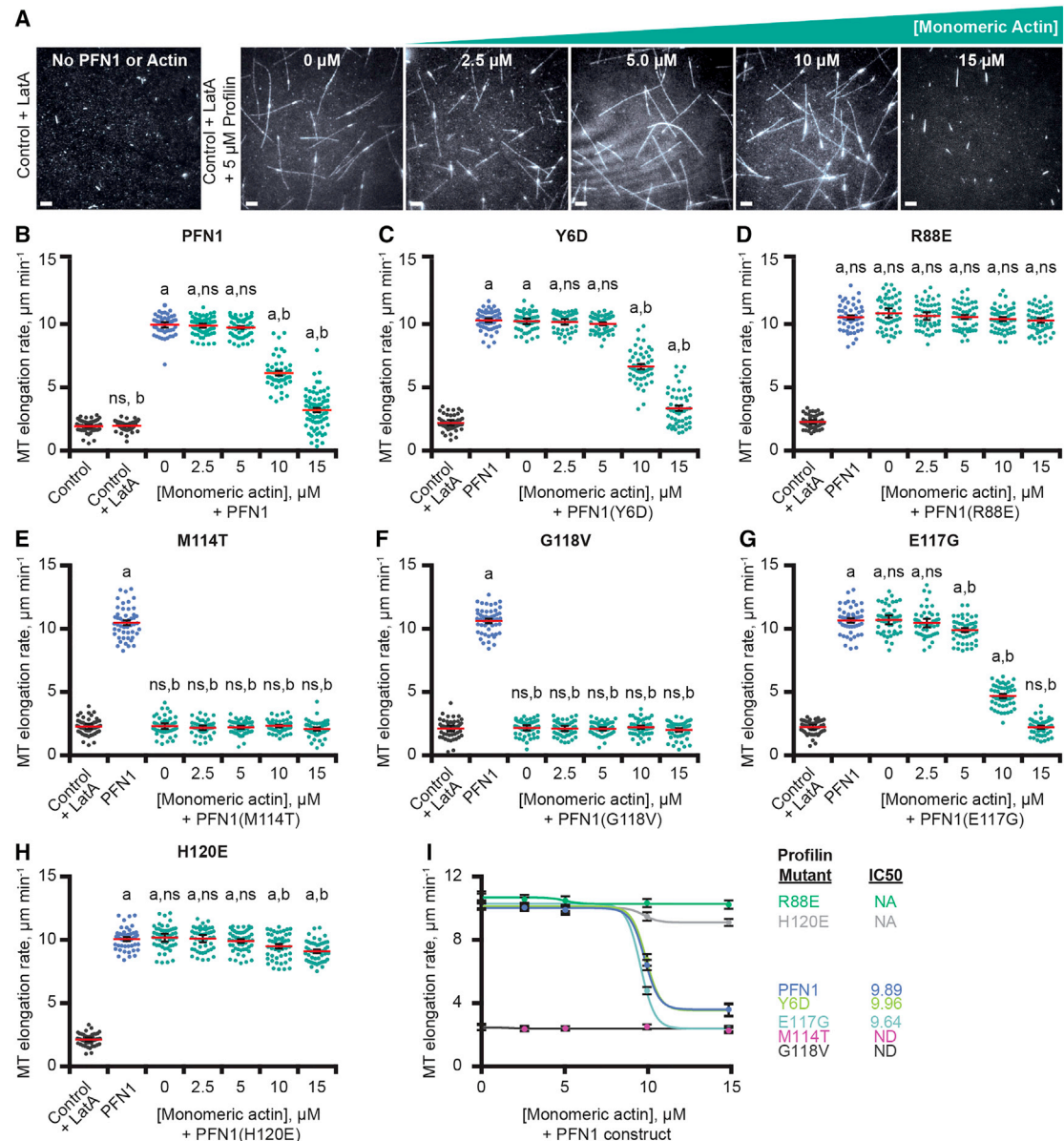See also Figures S1 and S2 and Movie S1.

Figure 3. Profilin Effects on Microtubules Are Attenuated with the Presence of Actin Monomers

(A) Representative views from TIRF assays containing biotinylated GMP-CPP MT seeds, 10 μM free tubulin (30% Alexa-647-labeled), 5 μM wild-type PFN1, and variable concentrations of monomeric actin bound to Latrunculin A (LatA). Scale bars, 10 μm.

(B–H) MT elongation rates for TIRF conditions described in (A) in the presence of 5 μM wild-type PFN1 (B), Y6D PFN1(C), R88E PFN1 (D), M114T PFN1 (E), G118V PFN1 (F), E117G PFN1 (G), and H120E PFN1 (H) (n = 50 MTs per condition). The presence of LatA (without actin) did not alter MT dynamics (B–H).

(I) Summary of dose-dependent loss of MT growth-enhancing effects for each profilin mutant in the presence of actin monomers generated from data in (B)–(H). All experiments were performed at least three times. Error bars indicate 95% confidence intervals. Significant differences by one-way ANOVA with Bartlett's correction for variance: ns, not significantly different from control; a, compared with control containing LatA ($p < 0.05$); b, compared with 5 μM wild-type PFN1 ($p < 0.05$).

See also Figure S3.

actin-binding impaired R88E mutant (Figure 4B). These results mirror our *in vitro* observations and demonstrate that profilin can increase MT growth rates in cells.

Next, we investigated the effects of elevated PFN1 expression on filopodial extension, a process regulated by MT-actin crosstalk [27–29]. Using live cell imaging to simultaneously monitor MT plus-ends (EB1-GFP) and actin filaments (mCherry-Utrophin), we examined the effects of PFN1 on MT penetrance into filopodia, average number of filopodia per cell, and filopodial stability (Figures 4C–4F). Wild-type PFN1 expression led to a significant increase in MT entry into filopodia (Figure 4D), as well as an increase in the number of filopodia per cell (Figure 4E) and average
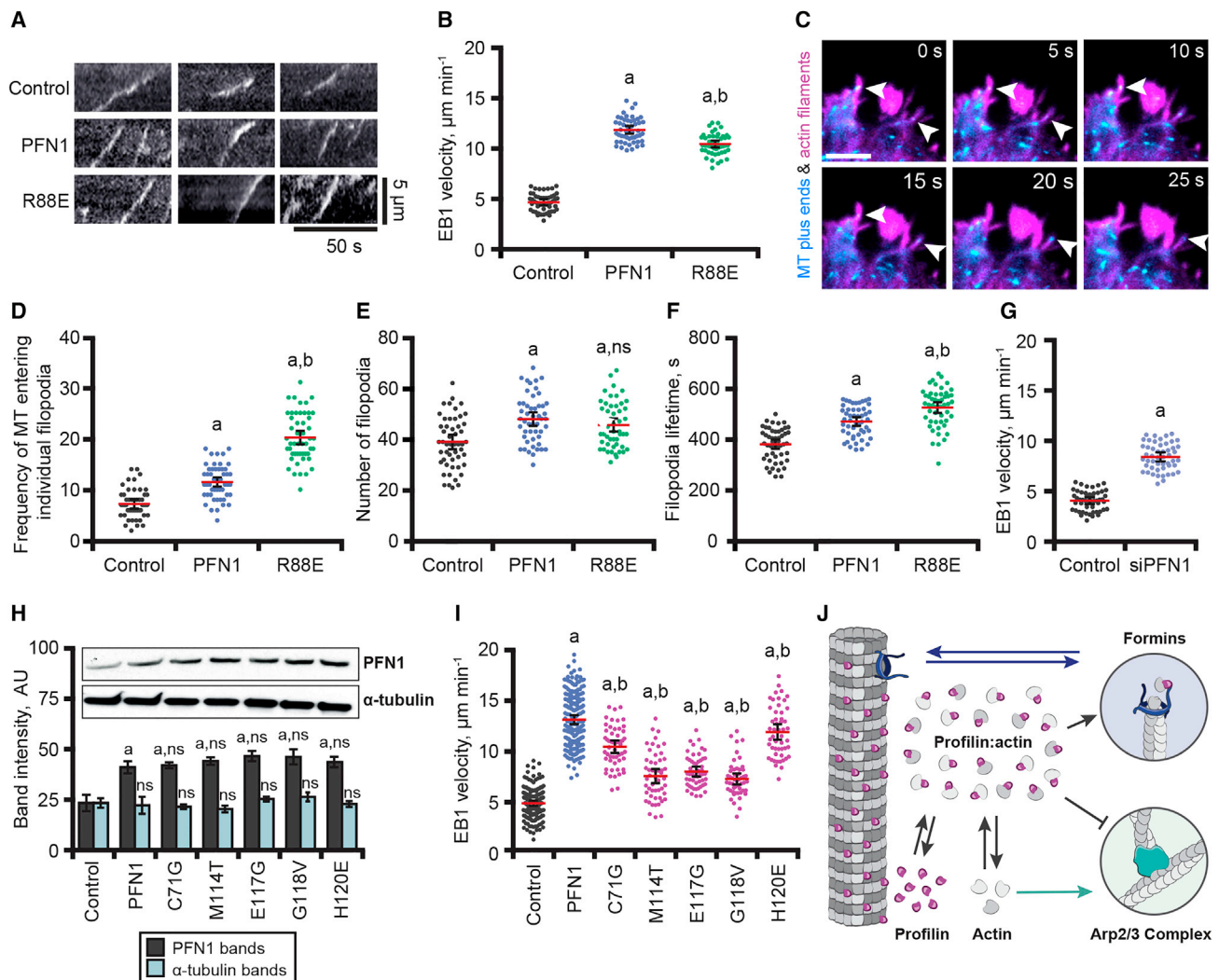
Figure 4. Cellular Effects of Wild-Type on MT Dynamics

(A) Representative kymographs generated from live-cell tracking of EB1-GFP comets from control cells and cells expressing wild-type or mutant PFN1 incapable of binding actin monomers (R88E) (n = 50–193 cells per condition). Length scale bar, 5 μm. Time scale bar, 50 s.

(B) Quantitative tracking analysis of EB1-GFP velocities from live-cell TIRF microscopy. Each data point graphed is the mean EB1-GFP velocity for a single cell, averaged from >3,000 EB1-GFP comets tracked during a period of 10 min.

(C) TIRF montage displaying the localization of actin (mChr-utrophin) and MT plus-ends (EB1-GFP) in filopodia at the cell periphery. Scale bar, 10 μm.

(D) Instances of MTs entering filopodia denoted by EB1-GFP (arrowheads) were counted over the lifetime of filopodia. EB1-GFP comets were present in individual filopodia were scored over the 10 min imaging period (n = 50 filopodia from 10 cells per condition).

(E and F) Number of filopodia (n = 30–50 cells) (E) and filopodia lifetimes (n = 250 filopodia from 10 cells per condition) (F).

(G) Live-cell EB1-GFP velocity tracking analysis from control or siPFN1 cells.

(H) Inset: western blots of cell extracts were used to determine relative PFN1 and α-tubulin levels for ALS-associated PFN1 mutants and controls. Quantification of band intensities from western blots of PFN1 levels (gray) and α-tubulin levels (teal) (n = 3 blots per treatment). Error bars represent SE.

(I) Live-cell TIRF microscopy of EB1-GFP comets was used to track MT plus-ends from control or cells with enhanced levels of PFN1 or PFN1 mutations associated with ALS (n = 50–193 cells per condition).

(J) Model for the distribution of profilin toward regulating actin or MTs. MTs, actin, and actin nucleators (formins and the Arp2/3 complex) compete for profilin. Thus, profilin is a molecular oscillator capable of regulating the dynamics of individual MTs, the availability of actin monomers to specific actin nucleation systems, and due to competition for profilin between MTs and actin monomers, acts as a regulator of actin-MT crosstalk. All experiments were performed at least three independent times. Error bars indicate 95% confidence intervals. Significant differences by one-way ANOVA with Bartlett's correction for variance: ns, not significantly different from control; a, compared with control ($p < 0.05$); b, compared with wild-type PFN1 ($p < 0.05$).

See also Figure S4 and Movie S3.

---

filopodial lifetime (Figure 4F). Expression of R88E PFN1 led to an increase in filopodia number similar to wild-type PFN1, but elicited an even greater increase in MTs entering filopodia and

average filopodial lifetime. These results suggest that the loss of actin binding in the R88E mutant may cause additional cytoskeletal defects that impact filopodial formation and stability,

possibly through profilin-formin interactions affecting the MT cytoskeleton [4, 21].

Our results demonstrate that a modest increase in PFN1 expression increases MT growth rates in N2A cells. However, a recent study showed that RNAi silencing of PFN1 in B16 melanoma cells also increases MT plus end velocities [4]. At first glance, these two observations seem to be at odds with each other. For this reason, we tested the effects of PFN1 silencing in our own system (Figures S4G–S4L). Similar to the results from B16 cells, we found that depletion of PFN1 in N2A cells led to an increase in MT velocity, albeit not to the same extent as cells with increased PFN1 expression (Figure 4G). Thus, MT growth rates appear to be highly sensitive to PFN1 levels in either direction, with either a >5-fold reduction in PFN1 or a ~2-fold increase in PFN1 producing faster MT growth rates. The increase in MT velocity in cells with slightly elevated PFN1 can be readily explained by our in vitro data showing that PFN1 directly binds and stimulates MT growth (Figures 1A and 1B). The less pronounced increase in MT velocity resulting from PFN1 silencing may be an indirect effect, stemming from the loss of profilin-formin interactions [4]. Therefore, these two effects appear to result from two separate mechanisms.

ALS-Linked Mutations in PFN1 Disrupt Microtubule Stimulatory Effects in Cells

Using the in vivo assays above, we finally asked whether the same ALS mutants defective in stimulating MT growth in vitro are also impaired in stimulating MT growth in cells. We individually expressed in cells the five ALS mutants (C71G, M114T, E117G, G118V, and H120E) and wild-type PFN1 and compared their effects on MT growth using EB1-GFP tracking (Movie S3). In each case, PFN1 levels approximately doubled, as indicated by quantitative immunofluorescence (Figures S4M and S4N) and western blot analysis (Figure 4H). Cellular levels of actin filaments and MTs were not significantly altered by wild-type or ALS mutant PFN1s (Figure S4O). Further, no difference in the total cellular tubulin levels was observed (Figures 4H and S4P), demonstrating that increased MT growth rates are not the result of higher tubulin concentrations. MT growth rates were enhanced similarly by wild-type PFN1 and the H120E mutant, which is impaired in actin binding (Figure 4I). C71G showed slightly weaker enhancement of MT growth, consistent its propensity to aggregate (Figure 4I) [7, 9]. M114T, E117G, and G118V were all impaired in stimulating MT growth, consistent with their in vitro activities (Figure 4I). Thus, our in vitro and in vivo observations are in good agreement showing that wild-type PFN1 promotes MT growth, whereas specific ALS-linked mutants are defective in these novel activities.

Conclusions

In vivo effects of profilin on MT dynamics and organization have been reported in systems ranging from mammalian cells to green algae and the protist T. cruzi [2, 30, 31]. Here, we demonstrated direct biochemical effects of human, yeast, and fly profilin homologs on MT dynamics, with each one enhancing the growth rate of MTs by several fold. In addition, we found that a modest 2-fold increase in the level of human profilin enhances MT growth rates, and these in vitro and in vivo effects on MT dynamics are disrupted by mutations in PFN1 linked to ALS. The MT regulatory res-

idues form a surface patch on profilin, which is distinct from, but adjacent to, the actin-binding surface. This proximity of these sites may explain why increasing levels of actin monomers competitively attenuate the stimulatory effects of PFN1 on MTs and why PFN1 mutants that impair actin-binding (R88E and H120E) render MT stimulatory effects unresponsive to actin monomers addition. Profilin and tubulin are both highly abundant in the cytosol, with estimated concentrations above 10 μM [32], making profilin well suited for governing cellular MT dynamics. Until now, estimations of the free versus actin monomer-bound fractions of profilin in cells have only considered competition with thymosin-β4 for actin monomer binding and have not considered the reciprocal possibility of factors competing with actin monomers for profilin binding. Our work reveals a competitive relationship between actin and MTs in binding profilin; therefore, a substantial fraction of profilin in cells may be bound to MTs. Indeed, tubulin and microtubule-associated proteins are among the major factors isolated from brain extracts on profilin affinity columns [19]. Further, a recent study showed that stabilization of the actin cytoskeleton with Jasplakinolide, which decreases actin monomer levels, increased PFN1 association with MTs in cells by immunofluorescence [4].

Profilin interactions in living cells may be more complex than previously appreciated (Figure 4J), and our data suggest that profilin not only mediates crosstalk between different actin nucleation systems [13, 14, 33], but also between MT and actin polymer systems. At present, we do not have a good assay for testing whether endogenous profilin influences MT dynamics through the direct mechanism we have reported. However, we observed strong stimulatory effects on MT growth rate in vitro at concentrations of MTs, profilin, and non-sequestered actin monomers close to estimated cellular conditions. Even though the cytosol of vertebrate cells contains ~100 μM actin monomers, most of this pool is bound to thymosin-β4, potentially increasing the cytosolic concentration of free profilin available to regulate MTs.

Our results also offer new insights into how specific ALS-linked mutations in PFN1 ultimately lead to motor neuron degeneration. We showed that three conserved residues on PFN1 mutated in ALS patients, which have little effect on PFN1-actin interactions [9, 10], (M114, E117, and G118), are critically involved in enhancing MT growth both in vitro and in cells. These results suggest that the progressive degeneration of motor neurons in ALS patients with these mutations may result from changes in the MT cytoskeleton. Further, they add to an increasing body of evidence suggesting that various defects in MT dynamics and MT-dependent axonal transport lead to motor neuron degeneration in ALS [34], including those caused by mutations in dynein, kinesin, and tubulin itself [35, 36]. In addition, some of the more common ALS-linked mutations such as in the RNA processing proteins TDP43 and FUS alter MT-dependent mRNA transport along motor neuron axons, and mutations in the ALS risk factor VEGF reduce the levels of MT-stabilizing microtubule-associated proteins [37]., Additionally, mutations in SOD1, which cause approximately twenty percent of all familial ALS cases, result in hyper-dynamic MTs and impaired axonal transport. Moreover, these defects are ameliorated by pharmacological stabilization of MT dynamics [38]. Thus, it is becoming increasingly apparent that MTs are a site of convergence in ALS,

impacted by diverse genetic insults linked to the disease, and chemically targeting MTs may be an effective approach for combating the lethality of ALS.

STAR★METHODS

Detailed methods are provided in the online version of this paper and include the following:

- KEY RESOURCES TABLE
- CONTACT FOR REAGENT AND RESOURCE SHARING
- EXPERIMENTAL MODEL AND SUBJECT DETAILS
- METHOD DETAILS
  - Reagents
  - Protein purification
  - *In vitro* TIRFM of microtubule dynamics
  - *In vitro* microtubule binding assays
  - Cell culture and image analysis
  - Western blotting
- QUANTIFICATION AND STATISTICAL ANALYSIS

AUTHOR CONTRIBUTIONS

J.L.H.-R. and B.L.G. designed experiments and wrote the manuscript. J.L.H.-R. and M.A.J. performed and analyzed the experiments.

REFERENCES

1. Carlsson, L., Nyström, L.E., Sundkvist, I., Markey, F., and Lindberg, U. (1976). Profilin, a low-molecular weight protein controlling actin polymerisability. In Contractile Systems in Non-muscle Tissues, S.V. Perry, ed. (Elsevier/North-Holland Biomedical Press), pp. 39–49.

2. Witke, W. (2004). The role of profilin complexes in cell motility and other cellular processes. Trends Cell Biol. *14*, 461–469.

3. Bartolini, F., Moseley, J.B., Schmoranzer, J., Cassimeris, L., Goode, B.L., and Gundersen, G.G. (2008). The formin mDia2 stabilizes microtubules independently of its actin nucleation activity. J. Cell Biol. *181*, 523–536.

4. Nejedla, M., Sadi, S., Sulimenko, V., de Almeida, F.N., Blom, H., Draber, P., Aspenström, P., and Karlsson, R. (2016). Profilin connects actin assembly with microtubule dynamics. Mol. Biol. Cell *27*, 2381–2393.

5. Wu, C.-H., Fallini, C., Ticozzi, N., Keagle, P.J., Sapp, P.C., Piotrowska, K., Lowe, P., Koppers, M., McKenna-Yasek, D., Baron, D.M., et al. (2012). Mutations in the profilin 1 gene cause familial amyotrophic lateral sclerosis. Nature *488*, 499–503.

6. Chen, Y., Zheng, Z.-Z., Huang, R., Chen, K., Song, W., Zhao, B., Chen, X., Yang, Y., Yuan, L., and Shang, H.-F. (2013). PFN1 mutations are rare in Han Chinese populations with amyotrophic lateral sclerosis. Neurobiol. Aging *34*, 1922.e1-5.

7. Freischmidt, A., Schöpflin, M., Feiler, M.S., Fleck, A.-K., Ludolph, A.C., and Weishaupt, J.H. (2015). Profilin 1 with the amyotrophic lateral sclerosis associated mutation T109M displays unaltered actin binding and does not affect the actin cytoskeleton. BMC Neurosci. *16*, 77.

8. Matsukawa, K., Hashimoto, T., Matsumoto, T., Ihara, R., Chihara, T., Miura, M., Wakabayashi, T., and Iwatsubo, T. (2016). Familial amyotrophic lateral sclerosis-linked mutations in profilin 1 exacerbate TDP-43-induced degeneration in the retina of *Drosophila melanogaster* through an increase in the cytoplasmic localization of TDP-43. J. Biol. Chem. *291*, 23464–23476.

9. Boopathy, S., Silvas, T.V., Tischbein, M., Jansen, S., Shandilya, S.M., Zitzewitz, J.A., Landers, J.E., Goode, B.L., Schiffer, C.A., and Bosco, D.A. (2015). Structural basis for mutation-induced destabilization of profilin 1 in ALS. Proc. Natl. Acad. Sci. USA *112*, 7984–7989.

10. Schutt, C.E., Myslik, J.C., Rozycki, M.D., Goonesekere, N.C.W., and Lindberg, U. (1993). The structure of crystalline profilin-β-actin. Nature *365*, 810–816.

11. Wolven, A.K., Belmont, L.D., Mahoney, N.M., Almo, S.C., and Drubin, D.G. (2000). In vivo importance of actin nucleotide exchange catalyzed by profilin. J. Cell Biol. *150*, 895–904.

12. Ezezika, O.C., Younger, N.S., Lu, J., Kaiser, D.A., Corbin, Z.A., Nolen, B.J., Kovar, D.R., and Pollard, T.D. (2009). Incompatibility with formin Cdc12p prevents human profilin from substituting for fission yeast profilin: insights from crystal structures of fission yeast profilin. J. Biol. Chem. *284*, 2088–2097.

13. Rotty, J.D., Wu, C., Haynes, E.M., Suarez, C., Winkelman, J.D., Johnson, H.E., Haugh, J.M., Kovar, D.R., and Bear, J.E. (2015). Profilin-1 serves as a gatekeeper for actin assembly by Arp2/3-dependent and -independent pathways. Dev. Cell *32*, 54–67.

14. Suarez, C., Carroll, R.T., Burke, T.A., Christensen, J.R., Bestul, A.J., Sees, J.A., James, M.L., Sirotkin, V., and Kovar, D.R. (2015). Profilin regulates F-actin network homeostasis by favoring formin over Arp2/3 complex. Dev. Cell *32*, 43–53.

15. Ferron, F., Rebowski, G., Lee, S.H., and Dominguez, R. (2007). Structural basis for the recruitment of profilin-actin complexes during filament elongation by Ena/VASP. EMBO J. *26*, 4597–4606.

16. Pollard, T.D., Blanchoin, L., and Mullins, R.D. (2000). Molecular mechanisms controlling actin filament dynamics in nonmuscle cells. Annu. Rev. Biophys. Biomol. Struct. *29*, 545–576.

17. Blanchoin, L., Boujemaa-Paterski, R., Sykes, C., and Plastino, J. (2014). Actin dynamics, architecture, and mechanics in cell motility. Physiol. Rev. *94*, 235–263.

18. Mouneimne, G., Hansen, S.D., Selfors, L.M., Petrak, L., Hickey, M.M., Gallegos, L.L., Simpson, K.J., Lim, J., Gertler, F.B., Hartwig, J.H., et al. (2012). Differential remodeling of actin cytoskeleton architecture by profilin isoforms leads to distinct effects on cell migration and invasion. Cancer Cell *22*, 615–630.

19. Witke, W., Podtelejnikov, A.V., Di Nardo, A., Sutherland, J.D., Gurniak, C.B., Dotti, C., and Mann, M. (1998). In mouse brain profilin I and profilin II associate with regulators of the endocytic pathway and actin assembly. EMBO J. *17*, 967–976.

20. Bender, M., Stritt, S., Nurden, P., van Eeuwijk, J.M.M., Zieger, B., Kentouche, K., Schulze, H., Morbach, H., Stegner, D., Heinze, K.G., et al. (2014). Megakaryocyte-specific Profilin1-deficiency alters microtubule stability and causes a Wiskott-Aldrich syndrome-like platelet defect. Nat. Commun. *5*, 4746.

21. Szikora, S., Földi, I., Tóth, K., Migh, E., Vig, A., Bugyi, B., Maléth, J., Hegyi, P., Kaltenecker, P., Sanchez-Soriano, N., and Mihály, J. (2017). The formin

DAAM is required for coordination of the actin and microtubule cytoskeleton in axonal growth cones. J. Cell Sci. *130*, 2506–2519.

22. Figley, M.D., Bieri, G., Kolaitis, R.-M., Taylor, J.P., and Gitler, A.D. (2014). Profilin 1 associates with stress granules and ALS-linked mutations alter stress granule dynamics. J. Neurosci. *34*, 8083–8097.

23. Yang, C., Danielson, E.W., Qiao, T., Metterville, J., Brown, R.H., Jr., Landers, J.E., and Xu, Z. (2016). Mutant PFN1 causes ALS phenotypes and progressive motor neuron degeneration in mice by a gain of toxicity. Proc. Natl. Acad. Sci. USA *113*, E6209–E6218.

24. Wu, C.-H., Giampetruzzi, A., Tran, H., Fallini, C., Gao, F.-B., and Landers, J.E. (2017). A *Drosophila* model of ALS reveals a partial loss of function of causative human PFN1 mutants. Hum. Mol. Genet. *26*, 2146–2155.

25. Suetsugu, S., Miki, H., and Takenawa, T. (1998). The essential role of profilin in the assembly of actin for microspike formation. EMBO J. *17*, 6516–6526.

26. Morton, W.M., Ayscough, K.R., and McLaughlin, P.J. (2000). Latrunculin alters the actin-monomer subunit interface to prevent polymerization. Nat. Cell Biol. *2*, 376–378.

27. Schaefer, A.W., Kabir, N., and Forscher, P. (2002). Filopodia and actin arcs guide the assembly and transport of two populations of microtubules with unique dynamic parameters in neuronal growth cones. J. Cell Biol. *158*, 139–152.

28. Rodriguez, O.C., Schaefer, A.W., Mandato, C.A., Forscher, P., Bement, W.M., and Waterman-Storer, C.M. (2003). Conserved microtubule-actin interactions in cell movement and morphogenesis. Nat. Cell Biol. *5*, 599–609.

29. Schober, J.M., Komarova, Y.A., Chaga, O.Y., Akhmanova, A., and Borisy, G.G. (2007). Microtubule-targeting-dependent reorganization of filopodia. J. Cell Sci. *120*, 1235–1244.

30. Holzinger, A., Valenta, R., and Lütz-Meindl, U. (2000). Profilin is localized in the nucleus-associated microtubule and actin system and is evenly distributed in the cytoplasm of the green alga *Micrasterias denticulata*. Protoplasma *212*, 197–205.

31. Osorio-Méndez, J.F., Vizcaíno-Castillo, A., Manning-Cela, R., Hernández, R., and Cevallos, A.M. (2016). Expression of profilin in *Trypanosoma cruzi* and identification of some of its ligands. Biochem. Biophys. Res. Commun. *480*, 709–714.

32. Koestler, S.A., Rottner, K., Lai, F., Block, J., Vinzenz, M., and Small, J.V. (2009). F- and G-actin concentrations in lamellipodia of moving cells. PLoS ONE *4*, e4810.

33. Henty-Ridilla, J.L., and Goode, B.L. (2015). Global resource distribution: allocation of actin building blocks by profilin. Dev. Cell *32*, 5–6.

34. Clark, J.A., Yeaman, E.J., Blizzard, C.A., Chuckowree, J.A., and Dickson, T.C. (2016). A case for microtubule vulnerability in amyotrophic lateral sclerosis: altered dynamics during disease. Front. Cell. Neurosci. *10*, 204.

35. Smith, B.N., Ticozzi, N., Fallini, C., Gkazi, A.S., Topp, S., Kenna, K.P., Scotter, E.L., Kost, J., Keagle, P., Miller, J.W., et al.; SLAGEN Consortium (2014). Exome-wide rare variant analysis identifies TUBA4A mutations associated with familial ALS. Neuron *84*, 324–331.

36. Williamson, T.L., and Cleveland, D.W. (1999). Slowing of axonal transport is a very early event in the toxicity of ALS-linked SOD1 mutants to motor neurons. Nat. Neurosci. *2*, 50–56.

37. Brockington, A., Heath, P.R., Holden, H., Kasher, P., Bender, F.L.P., Claes, F., Lambrechts, D., Sendtner, M., Carmeliet, P., and Shaw, P.J. (2010). Downregulation of genes with a function in axon outgrowth and synapse formation in motor neurones of the VEGFdelta/delta mouse model of amyotrophic lateral sclerosis. BMC Genomics *11*, 203.

38. Fanara, P., Banerjee, J., Hueck, R.V., Harper, M.R., Awada, M., Turner, H., Husted, K.H., Brandt, R., and Hellerstein, M.K. (2007). Stabilization of hyperdynamic microtubules is neuroprotective in amyotrophic lateral sclerosis. J. Biol. Chem. *282*, 23465–23472.

39. Henty-Ridilla, J.L., Rankova, A., Eskin, J.A., Kenny, K., and Goode, B.L. (2016). Accelerated actin filament polymerization from microtubule plus ends. Science *352*, 1004–1009.

40. Burkel, B.M., von Dassow, G., and Bement, W.M. (2007). Versatile fluorescent probes for actin filaments based on the actin-binding domain of utrophin. Cell Motil. Cytoskeleton *64*, 822–832.

41. Schindelin, J., Arganda-Carreras, I., Frise, E., Kaynig, V., Longair, M., Pietzsch, T., Preibisch, S., Rueden, C., Saalfeld, S., Schmid, B., et al. (2012). Fiji: an open-source platform for biological-image analysis. Nat. Methods *9*, 676–682.

42. Applegate, K.T., Besson, S., Matov, A., Bagonis, M.H., Jaqaman, K., and Danuser, G. (2011). plusTipTracker: Quantitative image analysis software for the measurement of microtubule dynamics. J. Struct. Biol. *176*, 168–184.

43. Castoldi, M., and Popov, A.V. (2003). Purification of brain tubulin through two cycles of polymerization-depolymerization in a high-molarity buffer. Protein Expr. Purif. *32*, 83–88.

44. Groen, A.C., Ngyuen, P.A., Field, C.M., Ishihara, K., and Mitchison, T.J. (2014). Glycogen-supplemented mitotic cytosol for analyzing *Xenopus* egg microtubule organization. Methods Enzymol. *540*, 417–433.

45. Spudich, J.A., and Watt, S. (1971). The regulation of rabbit skeletal muscle contraction. I. Biochemical studies of the interaction of the tropomyosin-troponin complex with actin and the proteolytic fragments of myosin. J. Biol. Chem. *246*, 4866–4871.

STAR★METHODS

KEY RESOURCES TABLE

REAGENT or RESOURCE	SOURCE	IDENTIFIER
Antibodies		
Rabbit anti-Profilin1	Abcam	ab50667; RRID: AB_2163191
Mouse anti-α-Tubulin	Santa Cruz Biotech., Inc	sc-32292; RRID: AB_2110259
Donkey anti-rabbit AlexaFluor-488	Thermo Fisher Scientific	A21206; RRID: AB_2535792
Donkey anti-mouse AlexaFluor-649	Thermo Fisher Scientific	A31571; RRID: AB_162542
Biological Samples		
Bovine brains	Adams Farm, Athol, MA	Bovine tubulin
Rabbit hind-leg muscle	Pel-Freez	RMA
Chemicals, Peptides, and Recombinant Proteins		
Methylcellulose [4000 cP]	Sigma	M0512
mPEG-silane, MW 2,000	Laysan Bio	N/A
Biotin-PEG-silane, MW 3,400	Laysan Bio	N/A
Recombinant Human Profilin1 (PFN1)	Purified according to [11]	N/A
Recombinant Human PFN1 (Y6D)	D. Kovar; described in [12]	N/A
Recombinant Human PFN1 (R88E)	D. Kovar; described in [12]	N/A
Recombinant Human PFN1 (M114T)	Purified according to [11]	N/A
Recombinant Human PFN1 (E117G)	Purified according to [11]	N/A
Recombinant Human PFN1 (G118V)	Purified according to [11]	N/A
Recombinant Human PFN1 (H120E)	Purified according to [11]	N/A
Saccharomyces cerevisiae Profilin (*Pfy1*)	Purified according to [11]	N/A
Drosophila melanogaster Profilin (*Chickadee*)	M. Quinlan	N/A
Experimental Models: Cell Lines		
Mouse neuroblastoma (N2A) cells	ATCC	CCL-131
Oligonucleotides		
Primer sequence: Site-directed mutagenesis of PFN1 to generate R88E mutation in pGW1 vector: GCATGGATCTTGAAACCAA GAGCAC	This work	N/A
Recombinant DNA		
Plasmid: pGW1 CMV::Human Profilin-1 (WT)	[5]	N/A
Plasmid: pGW1 CMV::Human Profilin-1 (R88E)	This work	N/A
Plasmid: pGW1 CMV::Human Profilin-1 (C71G)	[5]	N/A
Plasmid: pGW1 CMV::Human Profilin-1 (M114T)	[5]	N/A
Plasmid: pGW1 CMV::Human Profilin-1 (E117G)	[5]	N/A
Plasmid: pGW1 CMV::Human Profilin-1 (G118V)	[5]	N/A
Plasmid: pGW1 CMV::Human Profilin-1 (H120E)	[5]	N/A
Plasmid: pET Human PFN1 (WT)	[9]	N/A
Plasmid: pET Human PFN1 (M114T)	[9]	N/A
Plasmid: pET Human PFN1 (E117G)	[9]	N/A
Plasmid: pET Human PFN1 (G118V)	[9]	N/A
Plasmid: pET Human PFN1 (H120E)	[9]	N/A
pCMV::EB1-eGFP-N1	AddGene 17234; [39]	EB1-GFP
pCS2+ CMV::mCherry-Utrophin Binding Domain	AddGene 26740; [40]	mChr-Utr
Software and Algorithms		
Fiji (ImageJ)	[41]	N/A
plusTipTracker	[42]	N/A

(Continued on next page)

REAGENT or RESOURCE	SOURCE	IDENTIFIER
MATLAB	Mathworks	N/A
GraphPad Prism 6	GraphPad Software	N/A
Adobe Illustrator CS6	Adobe Systems	N/A
Other		
Custom-μ-Slide VIO.1 flow chambers (0.1 mm × 17 mm × 1 mm)	Ibidi	μ-Slide flow chambers
120 μm double-sided tape	Grace Bio-Labs	double-sided tape

CONTACT FOR REAGENT AND RESOURCE SHARING

Further information and requests for resources and reagents should be directed to and will be fulfilled by the Lead Contact, Bruce Goode (goode@brandeis.edu).

EXPERIMENTAL MODEL AND SUBJECT DETAILS

Recombinant Human Profilin-1 (PFN1), and mutations, were expressed in *E. coli* BL21(DE3) cells and purified as previously described [11]. The immortalized neuroblastoma (N2A) cell line, derived from a male mouse, was obtained directly from ATCC and used to examine the biological effects of wild-type and ALS-relevant mutations in PFN1 on actin and microtubules in cells. N2A cells were grown at 37°C with 5% CO_2 in DMEM supplemented with 200 mM L-glutamine and 10% FBS.

METHOD DETAILS

Reagents
All materials were obtained from Sigma-Aldrich (St. Louis, MO) unless noted.

Protein purification
Proteins were purified and/or fluorescently labeled as described below. Tubulin [43] was purified from freshly obtained *Bovine* brains by three cycles of temperature-induced polymerization and depolymerization. Brains were rinsed in 1 × PBS, then mixed with one volume depolymerization buffer (50 mM MES (pH 6.6), 1 mM $CaCl_2$), homogenized in a blender, and precleared by centrifugation at 29,000 × g for 1 h at 4°C. To polymerize tubulin, one volume of HMPB (1 M PIPES (pH 6.9), 10 mM $MgCl_2$, 20 mM EGTA, 10 mM DTT) was added to the supernatant, along with a final concentration of 1.5 mM ATP and 0.5 mM GTP, and 1/3 volume of glycerol. This mixture was incubated at 37°C for 1 h, and then microtubules (MTs) were pelleted by centrifugation at 151,000 × g for 30 min at 37°C. To depolymerize the MTs, the pellets were resuspended in cold depolymerization buffer, and incubated on ice for 30 min, then precleared at 70,000 × g for 30 min at 4°C. The supernatant was harvested, and polymerization and depolymerization steps were repeated two more times, for a total of three cycles. On the final cycle, depolymerziation was carried out in cold BRB80 buffer (80 mM PIPES (pH 6.8), 1 mM $MgCl_2$, 1 mM EGTA), and then the tubulin was precleared at 104,000 × g for 30 min at 4°C, aliquoted, and frozen in liquid nitrogen. To label tubulin with AlexaFluor-647 [43, 44], polymerized MTs were incubated with a 20-fold molar excess of dye for 30 min at 37°C in labeling buffer (0.1 M NaHEPES (pH 8.6), 1 mM $MgCl_2$, 1 mM EGTA, 40% (v/v) glycerol). The reaction was then quenched with 2 × BRB80 supplemented with 100 mM $C_5H_8KNO_4$ and 40% (v/v) glycerol. Excess dye was removed by performing two cycles of MT polymerization/depolymerization as above, and then aliquoted and stored in M2B (80 mM PIPES (pH 6.8), 2 mM $MgCl_2$, 1 mM EGTA) at −80°C. AlexaFluor-647 GMP-CPP MT seeds [44] were polymerized by combining 15 μM unlabeled tubulin, 7.5 μM AlexaFluor-647 tubulin, and 0.5 mM GpCpp (Jenna Bioscience, Jena, Germany) and incubating for 30 min at 37°C. MT seeds were collected by centrifugation and resuspended in 1 × BRB80, aliquoted, and stored at −80°C.

Wild-type human and ALS mutant Profilin1 proteins [11] were expressed in BL21(DE3) cells. Cells were grown to OD_{600} = 0.5 at 37°C, then induced with IPTG for 3 h at 37°C. Pellets were resuspended in 50 mM Tris HCl (pH 8.0) and DNase I, and sonicated at 4°C. The cell lysate was clarified by centrifugation at 20,000 × g. The supernatant was passed over at QHighTrap column (GE Healthcare, Marlborough, MA) equilibrated in 50 mM Tris-HCl (pH 8.0), 1 M KCl, and the flow-through (containing Profilin) was collected and then applied to a Superdex 75 (10/300) gel filtration column (GE Healthcare) equilibrated in 50 mM Tris (pH 8.0), 50 mM KCl. Fractions containing Profilin were pooled, aliquoted, and stored at −80°C. Thawed Profilin aliquots were pre-cleared at 279,000 × g before use.

Rabbit skeletal muscle actin (RMA) [45] was purified from acetone powder, generated from frozen ground hind leg muscle tissue from young rabbits (PelFreez, Rogers, AR). Lyophilized acetone powder stored at −80°C was mechanically sheered in a chilled coffee grinder, resuspended in G-buffer (3 mM Tris-HCl (pH 8.0), 0.5 mM DTT, 0.2 mM ATP, 0.1 mM $CaCl_2$), and then cleared by centrifugation at 50,000 × g. Actin was polymerized from the supernatant overnight at 4°C by addition of 2 mM $MgCl_2$ and 0.5 mM ATP. F-actin was pelleted by centrifugation at 361,000 × g, and then depolymerized by dounce homogenization and dialysis against

G-buffer for 48 h at 4°C. Monomeric actin was then precleared at 435,000 × *g*, and loaded onto a HiPrep S200 (16/60) gel filtration column equilibrated in G-Buffer. Fractions containing actin were stored at 4°C. Actin from these fractions was pre-cleared at 279,000 × *g* before use.

Protein concentrations were determined by band densitometry from Coomassie-stained SDS-PAGE gels, compared to a BSA standard curve, quantified using a LI-COR Odyssey imaging system (LI-COR Biotechnology, Lincoln, NE).

In vitro TIRFM of microtubule dynamics

Glass coverslips and Total Internal Reflection Fluorescence Microscopy (TIRFM) flow cells were prepared as described [39]. Briefly, flow cells were assembled by adhering sonicated PEG-silane coated coverslips to μ-Slide VI0.1 (0.1 mm × 17 mm × 1 mm) flow chambers (Ibidi, Martinsried, Germany) with 120 μm thick double-sided tape (2.5 cm × 2 mm × 120 μm) (Grace Bio-Labs, Bend, OR) and five-minute epoxy resin (Devcon, Riviera Beach, FL). Flow cells were sequentially conditioned with the following filter-sterilized buffers for 30 s each: 1% BSA, 4 μg/mL streptavidin in 10 mM Tris-HCl (pH 8.0), 1% BSA, and 1 × BRB80 supplemented with 0.25% methylcellulose [4000 cP], 15 mM glucose, 20 μg/mL catalase, 100 μg/mL glucose oxidase, and 0.1 mM GTP, and adjusted to pH 6.8 with KOH. Time lapse TIRFM was performed using a Ti200 inverted microscope (Nikon Instruments, Melville, NY) equipped with 100 mW solid-state lasers (Agilent Technologies, Santa Clara, CA), a CFI Apo 60 × 1.49 N.A. oil-immersion TIRF objective (Nikon Instruments), an EMCCD camera with a pixel size of 0.267 μm (Andor Ixon, Belfast, Northern Ireland). Focus was maintained using the Perfect Focus System (Nikon Instruments), and frames were captured at 3 s intervals (20 ms exposure, 633 nm excitation, 10% laser power). Reactions were introduced into the flow chamber, mounted on the microscope stage and flow-through was achieved using a syringe pump (Harvard Apparatus, Holliston, MA). Time between initial mixing of proteins and the start of TIRF recording was 20-30 s. All reactions were performed at 35°C, maintained by a stage heater (Ibidi) and an objective heater (Andor Ixon). GMP-CPP MT seeds were tethered to the coverglass surface via an avidin-biotin conjugation system. The chamber was washed with 1 × BRB80 buffer, and then 10 μM tubulin (30% AlexaFluor-649 labeled) plus other premixed proteins were flowed in. Dynamic MT parameters were determined by analyzing TIRF movies in Fiji [41]. MT elongation rates were determined from the change in MT length divided by the time growing, expressed in microns per min. The duration of MT growth events was determined only for MTs actively elongating, (i.e., not those paused or depolymerizing).

In vitro microtubule binding assays

MT co-pelleting assays were performed using MTs assembled in buffer (50 mM HEPES (pH 6.8), 100 mM KCl, 1 mM DTT, 0.1 mM GTP) for 30 min at 35°C, and then stabilized with GMP-CPP. MTs were diluted to different final concentrations and incubated for 10 min at 35°C with 5 μM precleared wild-type or ALS mutant PFN1. MTs were then pelleted by ultracentrifugation for 5 min at 278,100 × *g* at 35°C. Supernatants and pellets were fractionated on 15% SDS-PAGE gels, stained with Coomassie Blue, and the band intensities measured using a LI-COR imaging system (LI-COR Biotechnology, Lincoln, NE). Affinities were determined by fitting the data to a one-site binding equation (Figures 1J and 2G).

For imaging PFN1 bound to MTs, reactions containing MTs alone or MTs and 5 μM PFN1 were chemically fixed by flowing in 0.1% glutaraldehyde to the TIRF chambers. After 5 min of flow-in, the cells were washed three times with 1% BSA in 1 × BRB80 buffer and incubated with 1:500 primary antibody ab50667 against Profilin-1 (Abcam, Cambridge, UK) for 5 min. Flow cells were then washed three times as above and incubated with 1:2000 donkey anti-rabbit AlexaFluor-488 A21206 (Thermo Fisher Scientific) for 5 min. MTs were visualized after seven washes with 1 × BRB80 buffer. Line scans in the secondary fluorescence channel (488) were used to quantify the percent of secondary antibody fluorescence along fifty MTs from reactions performed in the presence or absence of PFN1.

Cell culture and image analysis

Neuroblastoma (N2A) cells were grown in DMEM (Thermo Fisher Scientific, Carlsbad, CA) supplemented with 200 mM L-glutamine (Thermo Fisher Scientific) and 10% FBS. Transfections were performed using Lipofectamine 3000 (Thermo Fisher Scientific) according to manufacturer's instructions in plastic 6-well plates, using 77,000 cells and 100 ng plasmid per well. Following 24 h transfection, cells were replated onto acid-washed uncoated 3 × 1 × 1 mm glass coverslips (VWR International, Radnor, PA) and fixed 4-6 h later with 4% paraformaldehyde. Profilin and tubulin levels in cells were measured by immunofluorescence as follows. Fixed cells were permeabilized in 1 × PBS supplemented with 0.1% Triton X-100 and 0.1 M glycine, blocked for 1 h in 3% BSA (w/v) diluted in PBST (1 × PBS supplemented with 0.1% Tween (v/v)) and incubated with 1:500 primary antibody ab50667 against Profilin1 (Abcam, Cambridge, UK) and 1:1000 primary antibody sc-32292 against α-tubulin (Santa Cruz Biotechnology Inc., Santa Cruz, CA) for 16 h. Coverslips were washed with 1 × PBST and incubated for 1 h with a combination of: 1:2000 donkey anti-rabbit AlexaFluor-488 A21206 (Thermo Fisher Scientific), 1:2000 donkey anti-mouse AlexaFluor-649 A31571 (Thermo Fisher Scientific), and 1:500 AlexaFluor-568 phalloidin (Thermo Fisher Scientific). Coverslips were mounted with AquaMount (Thermo Fisher Scientific) and imaged by laser scanning confocal microscopy on an inverted Nikon Ti eclipse microscope (Nikon Instruments, Melville, NY) equipped with a single 100 mW solid-state laser and emission tuner for 488 nm, 543 nm, and 633 nm wavelengths, a Plan Apo 100 × 1.45 N.A. oil-immersion objective, a C2 imaging head (Nikon Instruments), and an EMCCD camera with a pixel size of 0.12 μm/pixel (Andor Ixon). Images were acquired using Nikon Elements software (version 4.30.02) with 4 × averaging as 10 μm stacks with 0.5 μm steps at 10% laser power. Maximum intensity projections and raw fluorescence values were measured using Fiji [41]. Fluorescence values were normalized to cell area and fold-change in protein levels was calculated compared to mock-transfected cells).

Live-cell imaging was performed using TIRF microscopy. Cells were transfected with a combination of plasmids expressing: EB1-GFP [39], the actin-binding domain of Utrophin fused to mCherry (mChr-Utr) [40], and Profilin constructs [5, 9, 12]. Transfected cells were plated as above. After 24 h, cells were replated on glass-bottom dishes (MatTek Corporation, Ashland, MA) and imaged after an additional 4-5 h. Imaging was performed in RPMI buffer (Thermo Fisher Scientific) supplemented with 20 mM HEPES (pH 7.4), 10% FBS, 20 mM L-glutamine, and 1 mM sodium pyruvate (Thermo Fisher Scientific). Transfection efficiencies were >70% for each construct. Imaging was performed at 35°C in individual dishes imaged for a maximum of 30 min. Time lapse TIRF imaging was performed using a Ti200 inverted microscope (described above; Nikon Instruments) with an additional 1.5 × zoom module (Nikon Instruments). Images were captured at 1 s intervals in series: 10 ms at 488 nm excitation and 10 ms at 543 nm excitation. All lasers were used at 10% power. MT velocities and lifetimes were determined by tracking all EB1-GFP comets using plusTipTracker utrack software (Version 2.1.3) [42] in MATLAB version R2015a (The MathWorks, Natick, MA). Each data point graphed (Figure 4I) represents the mean velocity in a single cell, averaged from >3,000 events that occur over the course of 10 min. TIRF microscopy was used to quantify the frequency of MT entry into filopodia, enumerated as the number of times EB1-GFP entered fifty randomly chosen filopodia over their lifetime, from ten cells (expressing EB1-GFP to visualize growing MT ends and mChr-Utr to illuminate the cell periphery). Filopodia number (total number of filopodia visible in a cell at a single time point) and lifetimes were scored. Only filopodia that could be observed from their early emergence to complete collapse were used in the lifetime analysis.

Western blotting

To measure PFN, α-tubulin levels in cells, cells were collected 12-18 h after transfection and incubated for 30 min at 4°C in lysis buffer (150 mM NaCl, 1.0% NP-40, 0.5% sodium deoxycholate, 0.1% SDS, 50 mM Tris, pH 7.5, 2 mM EDTA, 0.2 mM sodium orthovanadate, 20 mM β-glycerophosphate, 50 mM sodium fluoride, 1 mM PMSF, 1 mM DTT, and 1 × Roche complete protease inhibitor mixture). Samples were precleared by centrifugation at 16,500 × g for 30 min at 4°C, quantified by Bradford assay, and immunoblotted. Blots were probed with 1:1000 primary antibody ab50667 against Profilin1 (Abcam, Cambridge, UK) or 1:2000 primary antibody sc-32292 against α-tubulin (Santa Cruz Biotechnology Inc., Santa Cruz, CA) for 2h. Blots were then probed with secondary horseradish peroxidase antibodies (GE Healthcare), and proteins were detected using Pierce ECL Western Blotting Substrate detection kit (Thermo Fisher). Bands were quantified by densitometry using Fiji.

QUANTIFICATION AND STATISTICAL ANALYSIS

GraphPad Prism 6 (GraphPad Software, La Jolla, CA) was used for all data analyses and to perform all statistical tests. At least three technical replicates for each experiment were performed. Precise details about the experimental design, sample size, and tests of significances for individual experiments can be found in each figure legend. Statistical significance was using one-way ANOVA with Bartlett's correction for variance when the p value is lower than 0.05. Individual data points are included in each figure (where appropriate), no data criteria were used to specifically include or exclude presented data.

Supplemental Information

Profilin Directly Promotes Microtubule Growth

through Residues Mutated

in Amyotrophic Lateral Sclerosis

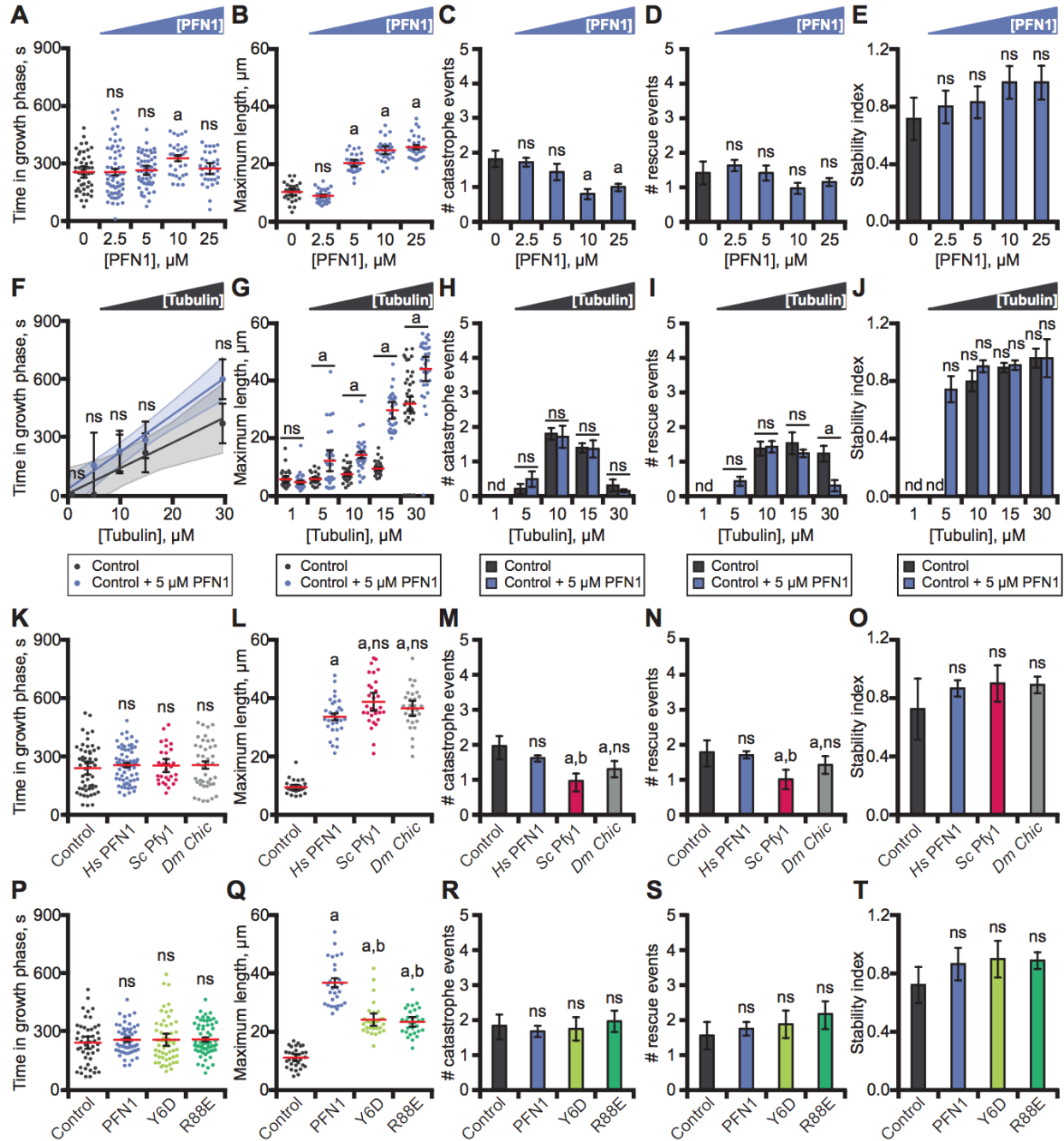Jessica L. Henty-Ridilla, M. Angeles Juanes, and Bruce L. Goode

Figure S1. PFN1 effects on microtubule dynamics in vitro. Related to Figure 1 and Figure 2.
(A) Duration of growth phase for individual MT elongation events (*n* = 47-62 MTs per condition) from TIRF reactions containing biotinylated GMP-CPP MT seeds, 10 μM free tubulin (30% Alexa-647 labeled), and variable concentrations of PFN1. **(B)** Maximum length MTs grew over a 20 min observation window (*n* = 32-51 MTs per condition). **(C** and **D)** Mean number of catastrophe or rescue events per MT (*n* = 30 MTs per condition). **(E)** MT stability index: rescue/catastrophe (*n* = 30 MTs per condition). Error bars in indicate SE. **(F)** Linear regression of the duration of growth phase for individual MT elongation events from TIRF assays as in (A), but with variable concentrations of free tubulin, in the presence and absence of 5 μM PFN1 (*n* = 30-73 MTs per condition). Shaded areas represent 95% confidence intervals and error bars indicate SE. **(G-J)** Parameters of MT dynamics analyzed from TIRF reactions as in (A) with variable concentrations of free tubulin, in the presence and absence of 5 μM PFN1 (*n* = 30-83 MTs per condition).

Catastrophe, rescue and stability index values were not determined (nd) for reactions where no dynamic MTs were observed (1 µM tubulin and 1 µM tubulin with 5 µM PFN1). Error bars indicate SE. **(K-T)** Parameters of MT dynamics analyzed from TIRF reactions as in (A) in the presence and absence of 5 µM wildtype human PFN1 (blue), *S. cerevisiae* Profilin (Pfy1) (pink), *D. melanogaster* Profilin (*Chickadee*) (grey), human PFN1 mutant Y6D (Chartreuse), and human PFN1 mutant R88E (green) (n = 30-83 MTs per condition). Error bars in (O and T) indicate SE. All experiments above were performed at least three times. Error bars indicate 95% confidence intervals except where noted. Significant differences by one-way ANOVA with Bartlett's correction for variance: ns, not significantly different from control; a, compared with control ($P < 0.05$); b, compared with PFN1 ($P < 0.05$).
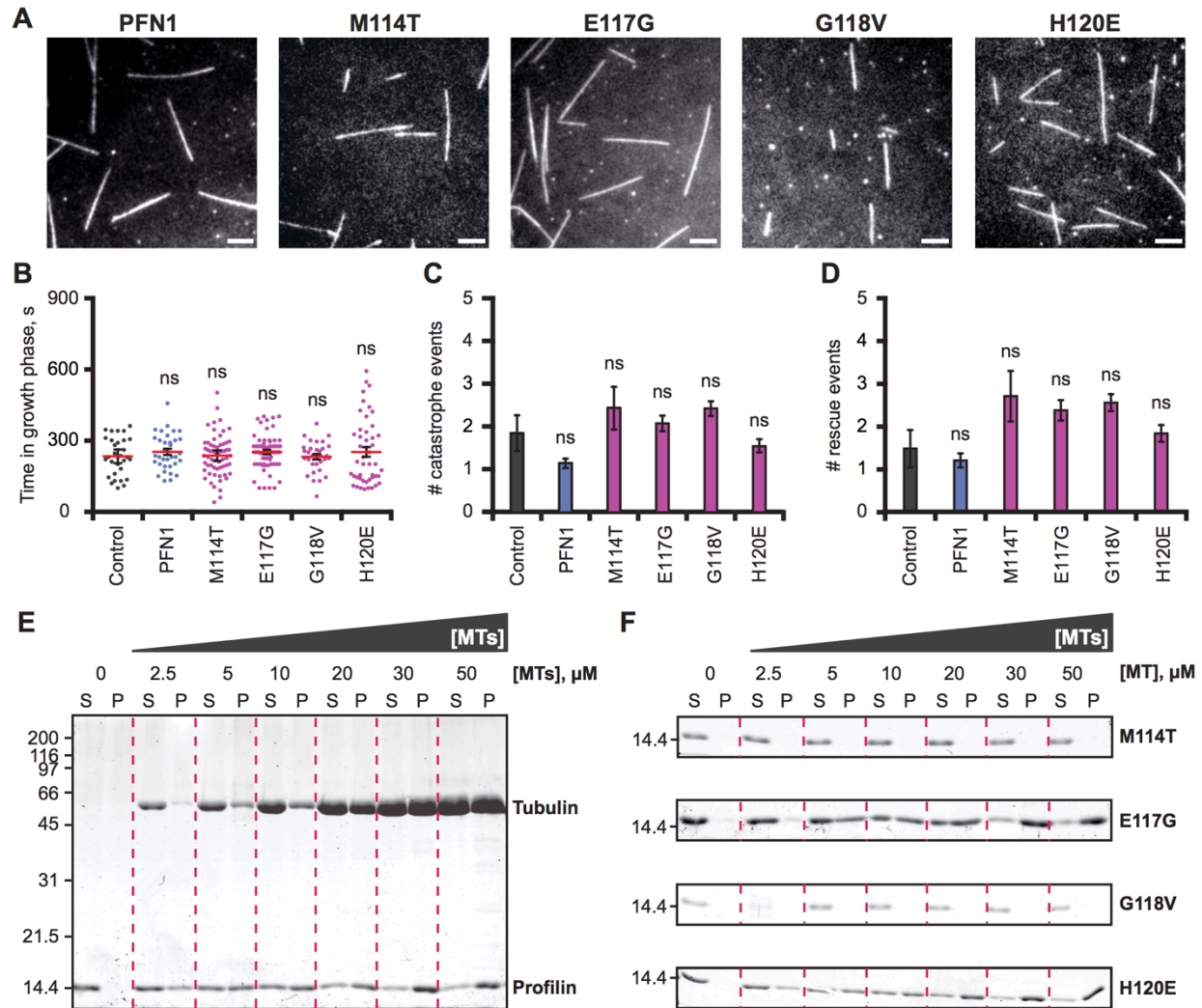
Figure S2. Microtubule interactions of wildtype and ALS-mutant PFN1 in vitro. Related to Figure 2.
(A) Representative fields of view from TIRF reactions containing biotinylated GMP-CPP MT seeds and 10 μM free tubulin (30% Alexa-647 labeled) in the absence (control) or presence of 5 μM wildtype or ALS-mutant PFN1s. Scale bars, 10 μm. Parameters of MT dynamics analyzed from TIRF reactions as in (A) including: **(B)** the time MTs spent growing (n = 50 MTs per condition); **(C)** mean number of catastrophe events per MT during a 20 min window (n = 30 MTs per condition); and, **(D)** mean rescue events per MT (n = 30 MTs per condition). Error bars in (D) indicate SE. All experiments were performed from at least three times. Error bars indicate 95% confidence intervals unless otherwise noted. Significant differences by one-way ANOVA with Bartlett's correction for variance: ns, not significantly different from control; a, compared with control (P < 0.05). **(E)** Coomassie-stained SDS-PAGE gel of supernatants and pellets from a co-sedimentation assay containing 5 μM wildtype PFN1 and variable concentrations (0-50 μM) of MTs. **(F)** Representative gels in as in (E), for ALS-mutant PFN1 proteins.
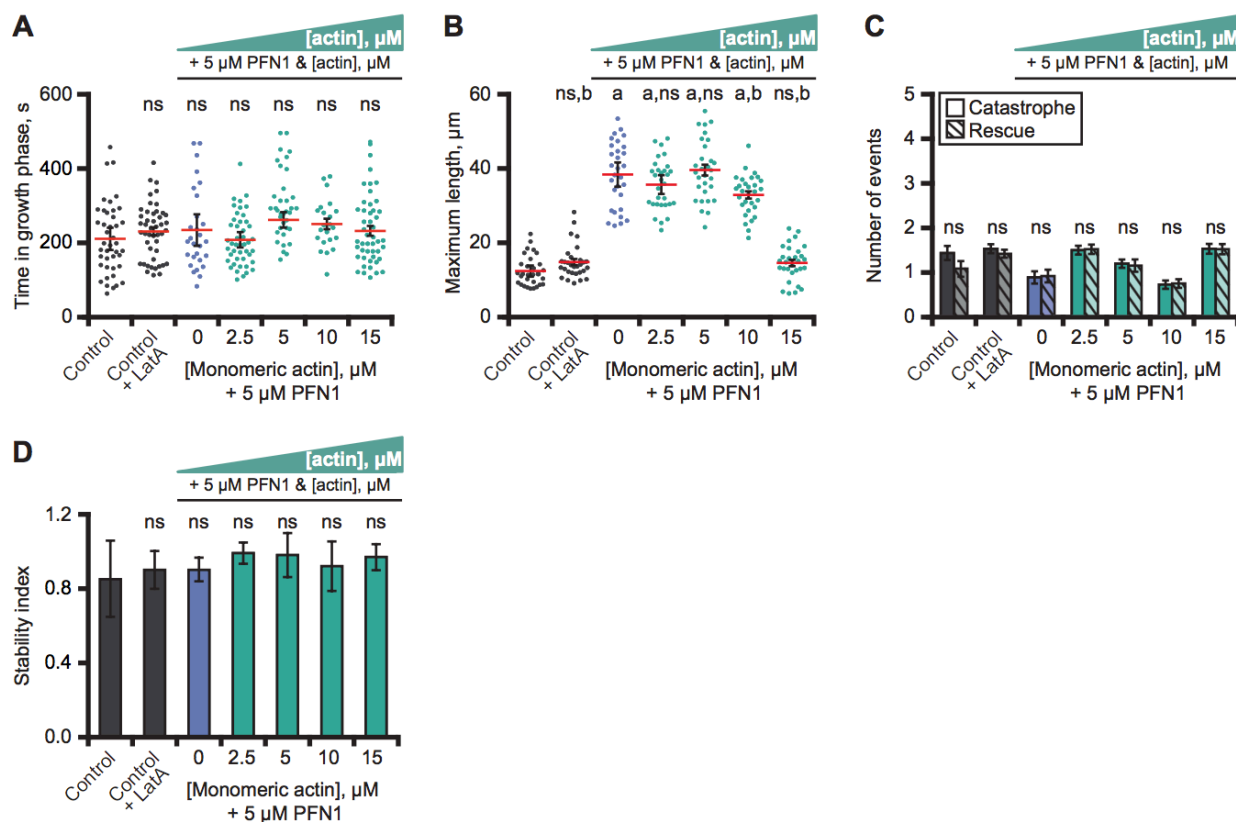
Figure S3. Effects of PFN1 on microtubule dynamics in the presence of actin monomers. Related to Figure 3.

Parameters of MT dynamics from TIRF reactions containing: 10 µM free tubulin (30% Alexa-647 labeled), 5 µM PFN1, and variable concentrations of monomeric actin bound to Latrunculin A (LatA). Parameters measured include: **(A)** the time MTs spent growing (n = 50-71 MTs per condition); **(B)** maximum length MTs grew to during the 20 min observation window (n = 30 MTs per condition); **(C)** mean number of catastrophe and rescue events per MT (n = 30 MTs per condition); and **(D)** MT stability index: rescue/catastrophe (measured from MTs in (C)). Note: the presence of LatA (without actin) had no significant effect on MT dynamics (A-D). Error bars indicate 95% confidence intervals, except for (C and D), which indicates SE. All experiments were performed at least three times. Significant differences by one-way ANOVA with Bartlett's correction for variance: ns, not significantly different from control; a, compared with control containing LatA without actin monomers ($P < 0.05$); b, compared with PFN1 without actin monomers ($P < 0.05$).
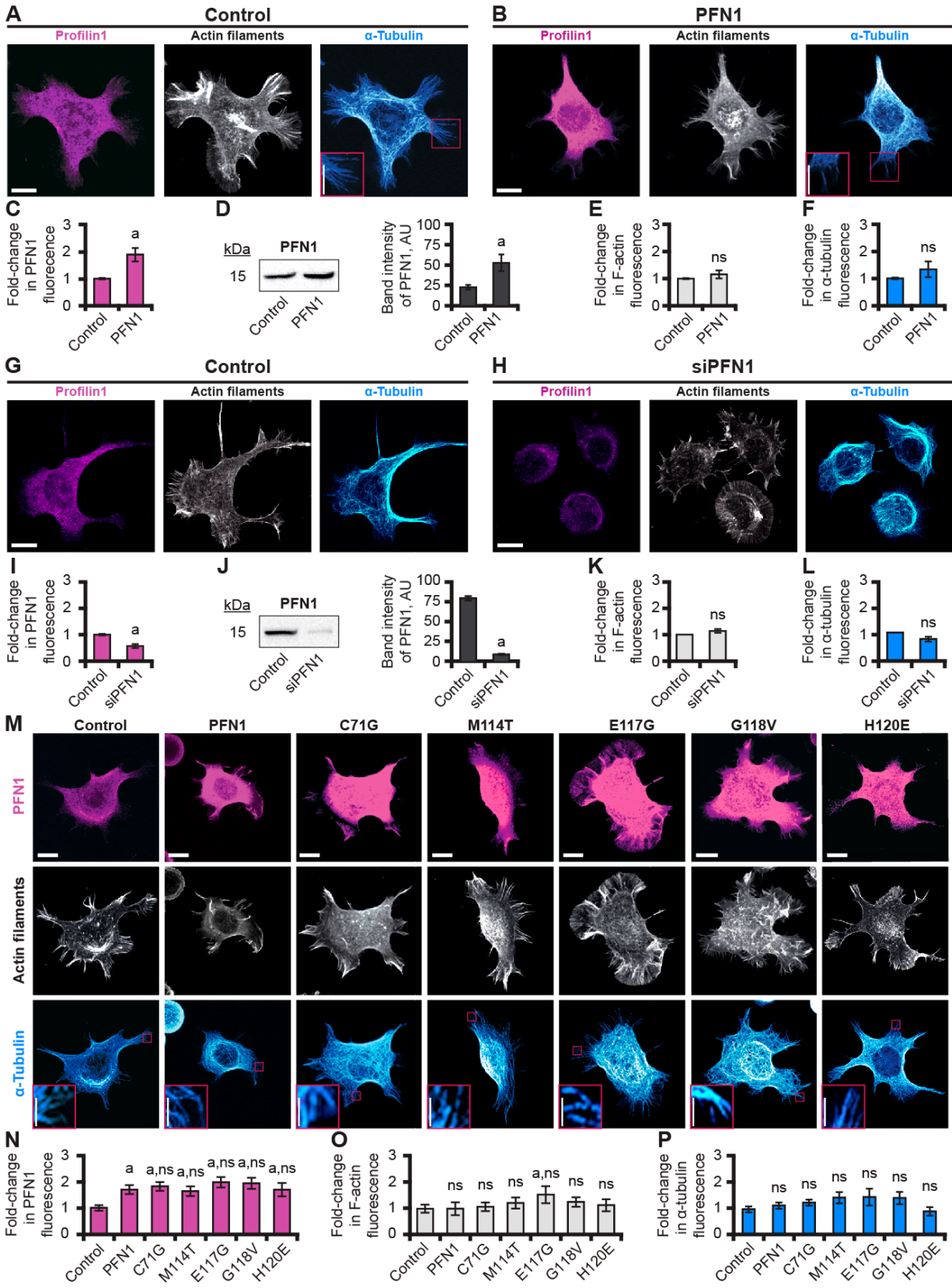
A Control
Profilin1 | Actin filaments | α-Tubulin

B PFN1
Profilin1 | Actin filaments | α-Tubulin

C
Fold-change in PFN1 fluorescence
a
Control | PFN1

D
kDa | PFN1
15
Control | PFN1
Band intensity of PFN1, AU
a
Control | PFN1

E
Fold-change in F-actin fluorescence
ns
Control | PFN1

F
Fold-change in α-tubulin fluorescence
ns
Control | PFN1

G Control
Profilin1 | Actin filaments | α-Tubulin

H siPFN1
Profilin1 | Actin filaments | α-Tubulin

I
Fold-change in PFN1 fluorescence
a
Control | siPFN1

J
kDa | PFN1
15
Control | siPFN1
Band intensity of PFN1, AU
a
Control | siPFN1

K
Fold-change in F-actin fluorescence
ns
Control | siPFN1

L
Fold-change in α-tubulin fluorescence
ns
Control | siPFN1

M
Control | PFN1 | C71G | M114T | E117G | G118V | H120E
PFN1
Actin filaments
α-Tubulin

N
Fold-change in PFN1 fluorescence
a | a,ns | a,ns | a,ns | a,ns | a,ns
Control | PFN1 | C71G | M114T | E117G | G118V | H120E

O
Fold-change in F-actin fluorescence
ns | ns | ns | a,ns | ns | ns
Control | PFN1 | C71G | M114T | E117G | G118V | H120E

P
Fold-change in α-tubulin fluorescence
ns | ns | ns | ns | ns | ns
Control | PFN1 | C71G | M114T | E117G | G118V | H120E

Figure S4. Effects of silencing PFN1 or expressing wildtype versus mutant PFN1 proteins in neuroblastoma cells. Related to Figure 4.

Confocal imaging of PFN1 immunofluorescence (magenta), actin filament staining by Alexa568-phalloidin (white), and tubulin immunofluorescence (cyan) in neuroblastoma (N2A) cells. Comparison of: **(A)** cells without an expression vector (control) and **(B)** cells expressing wildtype PFN1. Relative levels of PFN1 in N2A cells by **(C)** Immunofluorescence; and, **(D)** Western blot. The fluorescence intensity of **(E)** actin filaments stained with phalloidin; or **(F)** α-tubulin levels determined by antibody staining. Scale bars, 10 µm and inset scale bars, 5 µm. Red inset boxes display a zoomed view of peripheral MTs. Fluorescence was normalized to cell area (n = 68-113 cells for each condition). Confocal imaging of PFN1 immunofluorescence (magenta), Alexa568-phalloidin stained actin filaments (white), and tubulin immunofluorescence (cyan) from neuroblastoma (N2A) cells **(G)** without an expression vector, or **(H)** cells transfected with an siRNA construct that targets PFN1. **(I)** Immunofluorescence of PFN1 in endogenous and siPFN1 cells (n = 50 cells per condition) and **(J)** Western blots of cell extracts (n = 3 blots from cell extracts generated from separate transfections) were used to determine relative PFN1 levels. Error bars indicate SE. **(K-L)** Fluorescence intensity was used to measure relative levels of **(K)** actin filaments (n = 50 cells per condition) and **(L)** α-tubulin (n = 50 cells per condition). All cells measured by fluorescence intensity (panels I, K, L), were normalized to cell area. **(M)** Confocal imaging of PFN1 immunofluorescence (magenta), Alexa568-phalloidin stained actin filaments (white), and α-tubulin antibody staining from PFN1 cells without an expression vector (control), cells expressing wildtype or ALS-associated mutants of PFN1. Inset boxes display a zoomed view of peripheral MTs. **(N)** Quantification of PFN1 levels by immunofluorescence for cells as in (A) (n = 50 cells per condition). **(O-P)** Quantification of actin filament (F-actin) fluorescence by phalloidin staining (grey) and of α-tubulin immunofluorescence (cyan) for cells as in (A) (n = 50 cells per condition). Error bars indicate 95% confidence intervals. All experiments shown were performed in at least three independent trials. Significant differences by one-way ANOVA with Bartlett's correction for variance: ns, not significantly different from control; a, compared with control (P < 0.05); b, compared with wildtype PFN1 (P < 0.05).